Available online at www.sciencedirect.com
SCIENCE DIRECT®
International Journal of Heat and Mass Transfer 47 (2004) 5235–5245
International Journal of HEAT and MASS TRANSFER
www.elsevier.com/locate/ijhmt

Measurement of detailed heat transfer on a surface under arrays of impinging elliptic jets by a transient liquid crystal technique

W.M. Yan [a,*], S.C. Mei [a], H.C. Liu [a], C.Y. Soong [b], W.-J. Yang [c]

[a] Department of Mechatronic Engineering, Huafan University, Taipei 22305, Taiwan, ROC
[b] Department of Aerospace and System Engineering, Feng Chia University, Seatwen, Taichung 40724, Taiwan, ROC
[c] Department of Mechanical Engineering and Applied Mechanics, University of Michigan, Ann Arbor, MI 48109-2125, USA

Received 2 April 2004; received in revised form 11 June 2004

Abstract

Detailed heat transfer characteristics on a flat surface under arrays of impinging elliptic jets were measured by a transient liquid crystal technique. The elliptic jet holes of five different aspect ratios, AR = 4, 2, 1, 0.25, and 0.5, jet Reynolds numbers Re = 1500, 3000, and 4500, and three exit flow conditions are considered to investigate impingement heat transfer performance and the associated flow structure at various conditions. Results show that effects of the aspect ratio and crossflow have significant influences on the axial shift of the impingement/touchdown locations. The present thermographs with the high-Nu spots are very useful for understanding of the flow characteristics and jet structure deformation at various conditions. The axis-switchover phenomenon is found with the elliptic jets of aspect ratio AR > 1, but it does not occur in the cases of AR $\leqslant$ 1. Among the five aspect ratios considered, the mean heat transfer rates with the elliptic jets of AR = 0.5 are the highest at Re = 3000 and 4500; while, in the low-Re case of Re = 1500, the jet array with jet arrays with AR = 2 and 1 perform better than that with AR = 0.5. In addition, among the three, the two-way exit flow condition is most beneficial to the heat transfer characteristics of an impinging jet array.

1. Introduction

To enhance the heat exchange between fluid and a solid surface, various heat transfer augmentation techniques have been developed. Amongst, jet impingement is the effective means used in a variety of engineering applications, including the drying of film and textile, the cooling of gas turbine cooling, the tempering and annealing of glass, the thermal management of microelectronic components, etc.

Many studies have been performed to investigate the jet impingement heat transfer characteristics through numerical calculations and experiments [1,2]. In the previous literature, heat transfer enhancement with a single rectangular or round jet impinging on the surface was most extensively investigated. Empirical correlations of stagnation Nusselt number in terms of relevant dimensionless parameters were also surveyed in the literature. A single jet provides a particularly high heat/mass transfer performance in the stagnation region. For heat transfer associated with an array of impinging jets, the effects

* Corresponding author. Tel.: +886 2 2663 2102; fax: +886 2 2663 3173.
E-mail address: wmyan@huafan.hfu.edu.tw (W.M. Yan).

0017-9310/$ - see front matter © 2004 Elsevier Ltd. All rights reserved.
doi:10.1016/j.ijheatmasstransfer.2004.06.031

Nomenclature

a	radius of elliptic jet port in longitudinal direction of the channel
AR	aspect ratio of elliptic jet port, a/b
b	radius of elliptic jet port in transverse direction of the channel
d	hydraulic diameter of elliptic jet port
h	local heat transfer coefficient (W/m^{2}K)
h_m	mean heat transfer coefficient (W/m^{2}K)
k	thermal conductivity of acrylic material (W/m K)
k_f	air thermal conductivity (W/m K)
Nu	Nusselt number, hd/k_f
Nu_m	mean Nusselt number, $h_m d/k_f$
Pr	Prandtl number
Re	jet Reynolds number, Vd/v
T_i	initial temperature of the target surface (°C or K)
T_∞	mainstream temperature of the air flow (°C or K)
T_w	color change temperature of the liquid crystal, red-to-green (°C or K)
t	transient test time (s)
V	mean velocity of impinging jet (m/s)
X, x	dimensionless and dimensional axial distance of the target surface, $X = x/d$
Y, y	dimensionless and dimensional spanwise distance, $Y=y/d$
Z, z	dimensionless and dimensional spacing between jet plate and target plate, $Z = z/d$

Greek symbols

α	Thermal diffusivity of acrylic material (m^2/s)
v	Kinematic viscosity of air (m^2/s)
τ_j	Time step (s)

of the of jet array pattern, Reynolds number, crossflow, jet-to-target distance and their coupling effects significantly influence the flow and heat transfer characteristics. There exists a considerable body of literature dealing with the fluid flow and heat transfer characteristics under an array of air impinging jets [3–6]. In recent years, many investigators [7–9] have been explored heat transfer characteristics of an array of liquid impinging jets. They focused largely on the arrays for which crossflow effects, which potentially degrade the high stagnation heat transfer associated with impinging jets, are designed to be minimal.

Detailed heat transfer distributions under arrays of jets impinging on a target plate with dimpled or film hole surfaces were investigated by Treuren et al. [10] and Han and his colleagues [11–13] using a liquid crystal image technique. They found that the crossflow and the exit flow direction significantly affect the heat transfer distributions on a target surface. The results of Han's group [11–13] were, however, limited to jet array of inline pattern and only one fixed jet-to-plate spacing was considered. Carcasci [14] experimentally investigated air impinging jets on a flat plate. By using the results of smoke visualization, oil paint and liquid crystal techniques, vortex structure induced by the impinging jets were studied. Recently, Yan et al. [15] extended the previous experimental works [11–13] and measured the detailed local heat transfer distributions under impingement of inline and staggered jet arrays.

Non-circular jets have very interesting hydrodynamic characteristics that may have influences in mixing, entrainment and even heat transfer. Among the possible geometries, flow structure of elliptic jet has drawn lots of attentions, e.g., [16–19], in which the similarity in deformation of large scale vortical structure between the elliptic jet and the elliptic vortex ring has been demonstrated. The inherent instability involved causes a non-uniform self-induction mechanism and the two axes of the elliptic jet/ring are interchanged. This axis-switching mechanism may enhance the entrainment and mixing. As to the heat transfer characteristics associated with elliptic jets, Lee et al. [20] examined heat transfer of an elliptic impingement jet of aspect ratio AR = 2.14; while the effects of jet hole aspect ratio on the stagnation heat transfer performance were experimentally investigated by Lee and Lee [21].

The jet impingement heat transfer performance can be influenced by some flow and geometry parameters, e.g. jet Reynolds number, jet hole or port geometry, impinging channel height, exit flow orientation, etc. Most of the previous studies are pertaining to the heat transfer performance of a circular jet or jet array. In the previous studies on elliptic jets, to our best knowledge, impingement heat transfer with the presence of the crossflow effect was not reported yet. In the present study, the emphasis is therefore focused on the effects of the aspect ratio of elliptic jets and the spent-air crossflow orientation on the local heat transfer characteristics. The elliptic jet holes with aspect ratio AR = 4, 2, 1, 0.5 and 0.25 and the same hydraulic diameter $d = 10$ mm are to be tested for the jet-to-plate spacing of $Z = 3$. In addition, the effects of crossflow and exit flow orientations are investigated. To resolve the highly localized heat transfer distributions, a transient liquid crystal technique in connection with a thin film of thermochromic liquid crystal (TLC) coated directly on the impingement

target surface is employed to measure the local heat transfer distributions. During a transient test, the color change of TLC film on the target surface was monitored and recorded by an automatic computer vision system and a data acquisition system. The time of color change of the liquid crystals to green is measured using an image processing equipment.

2. Experimental set-up and procedure

2.1. Test apparatus and models

Fig. 1 presents a schematic diagram of the experimental apparatus. The experimental apparatus consists of an image-processing system, a blower, an electric heater, a honeycomb set, a plenum, a computerized data acquisition system, and a test section. The test section consists of two compartments separated by a jet plate with an array of elliptic holes of hydraulic diameter $d = 10$ mm on it. The top compartment is called pressure chamber, while the bottom compartment is the impingement channel. The air flow entering the pressure compartment go downward to impinge the target plate through the elliptic holes. On the jet plate, 9 (streamwise) $\times$ 3 (spanwise) jet holes are arranged in an in-line pattern. The center-to-center distance between two neighboring jet holes are $3d$ and $1.5d$ in the streamwise and spanwise directions, respectively. The inlet pressure chamber has a cross section of 100 mm $\times$ 50 mm.

The target plate is measured 300 mm $\times$ 100 mm $\times$ 10 mm in length $\times$ width $\times$ thickness. Five models of jet hole aspect ratios AR=a/b = 4, 2, 1, 0.5 and 0.25 are studied in this experimental work, where a and b, respectively, are the radii in longitudinal and transverse directions of the channel. The plenum is a 500 mm long chamber with cross section of 100 mm $\times$ 100 mm through which the flow develops before entering to the pressure chamber. The average jet velocity through each jet hole is measured by using a Pitot-tube.

The test section is made of transparent acrylic plates for accessing images by a camera. The impingement target surface is made of a black acrylic plate and coated with liquid crystal on the inside surface. The choice of the black acrylic is due to its low thermal conductivity. The test section is assembled after a thin film of the liquid crystal (Hallcrest, BW/R38C5W/C17–10) sprayed uniformly on the target surface. The computerized data acquisition system consists of a digital image processing system and a data logger. The image processing system used in this work is composed of a digital color camcorder (camera + image recorder, SONY DCR-TRV7), a frame grabber card, and a Pentium IV personal computer. The isotherms of red-to-blue transition band were captured through a digital color camcorder with resolution of 682 $\times$ 492 pixels. These captured images were digitized by a frame grabber and analyzed using image-processing software.

Fig. 2 presents the sketch of the three exit flow orientations with different flow discharge opening. As shown in Fig. 2, the flow orientation 1 is that the main flow enters the pressure chamber and exits the impingement channel in the same direction. In the case of the exit flow orientation 2, the flow enters the pressure chamber from

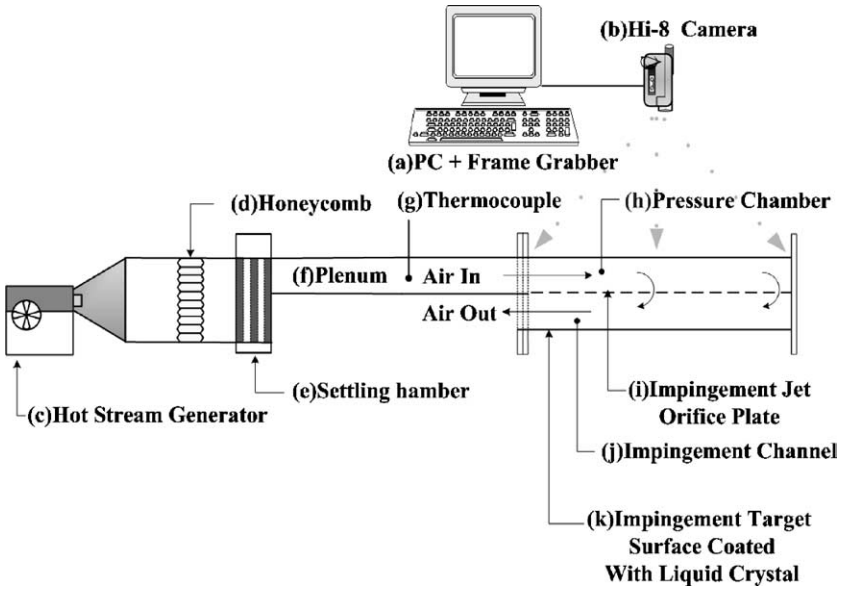

Fig. 1. Schematic diagram of the experimental apparatus.

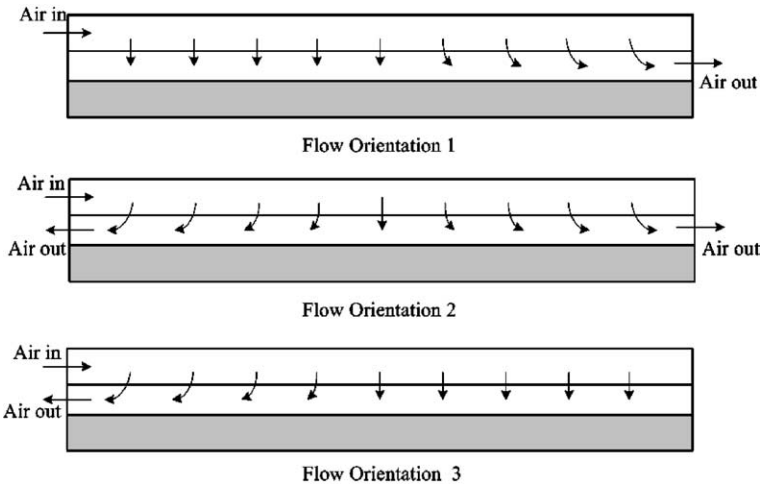

Fig. 2. Sketch of the channel with three exit flow orientations.

one end ($X = 0$) and exits the impingement channel from both ends ($X = 0$ and 30). For the flow orientation 3, the main flow goes through the impingement channel in opposite direction of the entry flow in the pressure chamber.

2.2. Experimental procedure

Since the actual color image can be affected from many factors such as the thickness and surface condition of liquid crystal, the angle of camera and lighting illuminator, a careful temperature calibration of liquid crystal has to be done in the preliminary test phase, in which the TLC and thermocouples with a FLUKE Helios Plus data logger were employed. The liquid crystal was calibrated using the digital image processing system under the same conditions of experimental runs, including the illuminating light and the camera-viewing angle under the conditions of the laboratory. In this work, the green color appears at 39.2 °C. During each test run, the air mass flow rate was set for the required Reynolds number. The air is heated by an electric heater in the blower section. At the exit of the heater, the air temperature is set based on the experience of test runs to produce acceptable time period for color-change response of the liquid crystal. The test section is ready for running when the air fan is switched on. Meanwhile, the data logger for temperature measurement and the image processing system are set to trigger for initiating data measurement at the same time instant. The image processing system records the transition time for the color changing into green, and transmits the data into a matrix of the time for color-change over the entire test surface. The data of time and temperature are input to a computer program to determine the local heat transfer coefficients. More detailed description of the experimental procedures is available in our previous studies [15,22].

3. Heat transfer theory

For the acrylic material used for model assembly, the heat penetrating depth into the plate over the time duration needed to complete one test run is less than the target plate thickness. In addition, it is expected that the lateral conduction in the plate have no significant effect on the local surface temperature response. Therefore, the test condition is assumed to be a one-dimensional transient conduction model through a semi-infinite solid with surface convection. The surface temperature can be expressed as

$$(T_w - T_i)/(T_\infty - T_i) = 1 - \exp(\gamma^2)\mathrm{erfc}(\gamma), \qquad \gamma = h\sqrt{\alpha t}/k \tag{1}$$

where T_i is the initial temperature of the test surface and the T_∞ stands for the jet flow temperature. The thermal diffusivity α and the thermal conductivity k of the Acrylic material are known a priori. In order to determine the local heat transfer coefficient h, the temperature T_w for the color of the liquid crystal-coated surface turning into green was determined based on the calibration test of temperature change of the liquid crystal. The corresponding time, t, to reach the temperature for a heat transfer surface is measured by using the image processing system. The time required for color change in a typical test run is about 15–90 s depending on the experimental conditions as well as the measurement locations.

However, the target surface will not actually experience a step change in the driving air temperature due to the transient heating of the upstream jet plate and

duct walls. Therefore, the solution in Eq. (1) must be modified to include the effect of the gradual change of the temperature in T_∞. Using Duhamel's superposition theorem, the solution in Eq. (1) can be expressed as

$$T_w - T_i = \sum_{j=1}^{n} \left\{ 1 - \exp\left[\frac{h^2\alpha(t-\tau_j)}{k^2}\right] \times \operatorname{erfc}\left[\frac{h\sqrt{\alpha(t-\tau_j)}}{k}\right] \right\} [\Delta T_{\infty j}] \quad (2)$$

where ΔT_∞ and τ_j, respectively, are the flow temperature change and the time step from the histogram of the jet flow temperature. In the present work, the jet flow temperature T_∞ is determined by thermocouple measurement in the pressure chamber prior to jet issuing. The variation of T_∞ with time is recorded and approximated by step changes. With the color change time t at any location, the resulting superposed solution, Eq. (2), is solved for the local heat transfer coefficients.

4. Results and discussion

4.1. Flow characteristics in pressure channel

Three exit flow orientations considered in the experiments are shown in Fig. 2. In abbreviation, hereafter, ExF-1, ExF-2, and ExF-3 are used in the text to designate the exit flow orientations 1, 2, and 3. The global flow rate is a control parameter related to the jet Reynolds number. To meet a real situation in applications, however, the local flow rate through the individual hole is not controlled artificially. The variation of the jet velocity from hole to hole along the longitudinal direction is examined for understanding of the flow behavior and the local flow rate accumulation along main flow direction in the impingement channel. Fig. 3(a) shows the longitudinal variation of the spanwise average of jet velocity for circular jet arrays (i.e., AR = 1) and Fig. 3(b) presents the corresponding local mass flow rate accumulated in the longitudinal (X) direction. Each local jet velocity is a transverse average of the three ports at each X-location at various conditions of exit flow. It is observed that the local velocities of both one-way exit cases, ExF-1 and ExF-3, are nearly linear along X-direction and the maximum variations are around 40%. Whereas the jet velocity with the two-way exit, ExF-2, is nearly uniform with hole-to-hole variation about 10%. Due to the addition of the local jet flow, the flow rate is accumulated almost linearly along the main flow direction. The axial distribution of local flow rate in Fig. 3(b) is of a linearly increasing pattern from nearly center (X = 12–15) of the channel to the ends. The distribution of the flow rate is a little asymmetric, which is attributed to the different left and right end conditions of the pressure channel. The left end of the pressure channel is an open inlet, while the right end is closed by a vertical end plate.

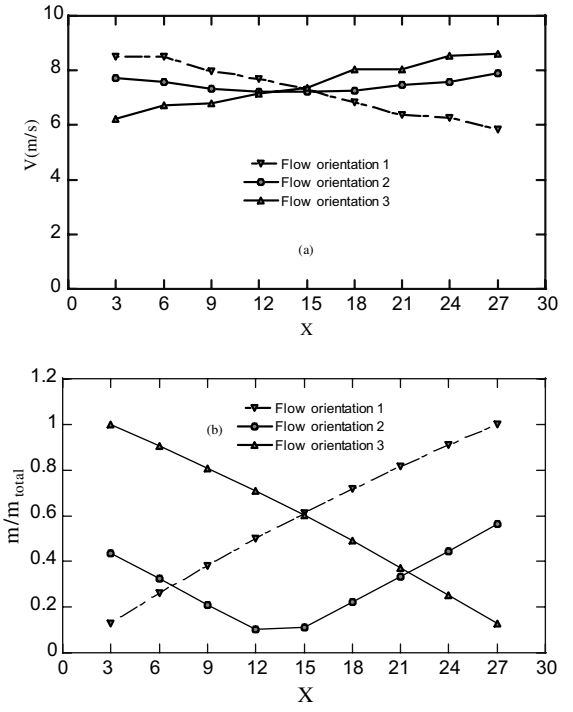

Fig. 3. Jet velocity and local mass flow rate along the channel axis.

4.2. Effects of exit flow condition for elliptic jets

The thermographs for the effects of flow orientations for the case of AR = 0.5 and AR = 2 are shown in Figs. 4 and 5, respectively. The arrows in the figures with the abscissa $X = 3, 6, 9, \ldots, 27$ indicate the axial locations of the jet holes. The heat transfer performance is characterized by the Nusselt number defined as $Nu = hd/K_f$. Each spot in the thermographs shows the touchdown location and the shape of an impinging jet, where the heat transfer rate appearing as a peak due to the impingement effect. In each thermograph in Figs. 4 and 5, touchdown location of each elliptic jet has an obvious shift from the location of the jet hole. For the cases of ExF-1 in Figs. 4(a), in the upstream portion of the impingement channel where the crossflow is weak, the locations of the high-Nu spots deviate only slightly from the corresponding jet hole locations. As the crossflow develops, the locations of the heat transfer peaks are significantly shifted downstream. The extent of the touchdown location shift is more remarkable in the case of spent-air flow having the same direction as the flow in the pressure channel. At the same exit flow condition, a jet hole of

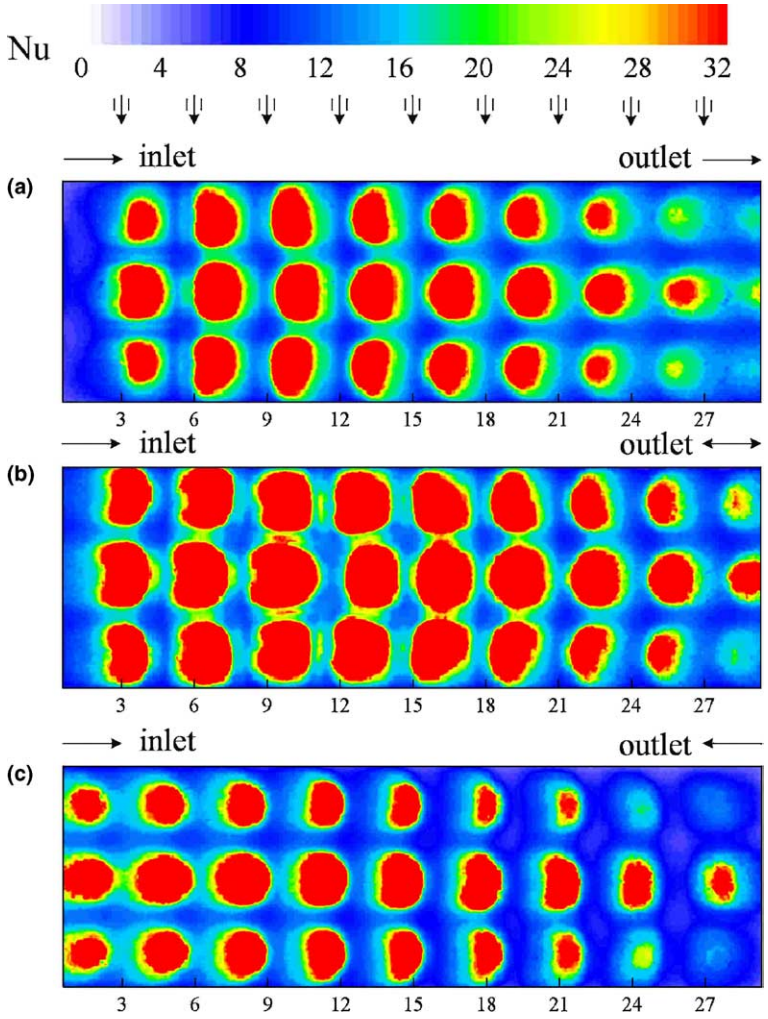

Fig. 4. Effects of flow orientation on local Nusselt number distributions at $Re = 3000$, $Z = 3$ and AR=0.5 with (a) ExF-1, (b) ExF-2, (c) ExF-3.

larger aspect ratio has its major axis in the longitudinal direction. The axial shift of the jet impingement location depends strongly on the axial momentum of the flow from the pressure channel. The mechanism can be explained by using the schematic diagrams in Fig. 6. In addition to the inertia effect, the crossflow is another influential factor to the jet trajectory. The shift increases with the increasing travel length of the crossflow, for which the stronger convection effect due to the accumulated flow in downstream part is the major reason. Accordingly, jets with the two-way exit, ExF-2, in Fig. 4(b) has relatively small shift. For the ExF-3 in Fig. 4(c), the flow enters the pressure channel at $X = 0$ and, after turning to go through the jet holes and impinging the target plate, exits the impingement channel at $X = 0$ along the opposite direction. Due to the crossflow effect, the axial distributions of the spanwise average Nu show a shift of the impingement location toward the exit direction ($X = 0$). The extent of the shift is more significant near the exit end ($X = 0$) due to the stronger crossflow effects.

In Fig 4, due to different crossflow effects, the distributions of the impinging spots and their shapes in the cases with three exit flow orientations are obviously different. In the case of ExF-2, relatively, the jet impinging effect performs the highest heat transfer rates among the three exit flow conditions, since in the latter case all the spent air exits from the channel center towards both ends and thus the heat transfer deterioration due to the crossflow effect is smallest. Different from the results of AR = 0.5 in Fig. 4, the data from the experiment with the elliptic jet holes of the major axis in mainstream

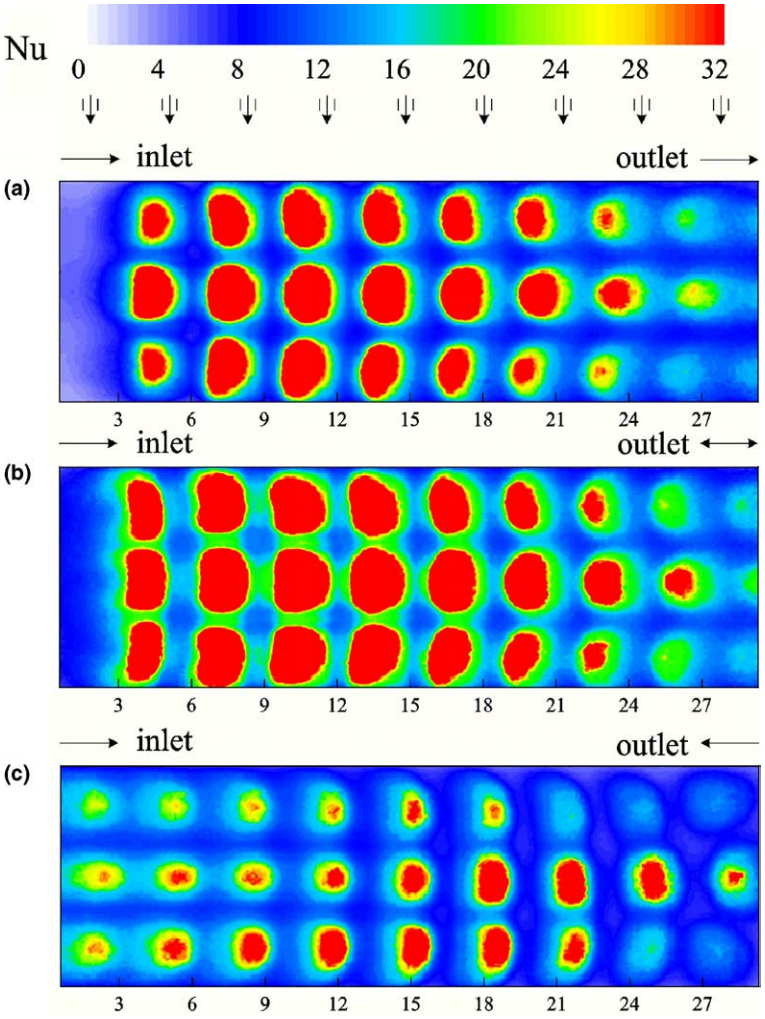

Fig. 5. Effects of flow orientation on local Nusselt number distributions at $Re = 3000$, $Z = 3$ and AR = 2 with (a) ExF-1, (b) ExF-2, (c) ExF-3.

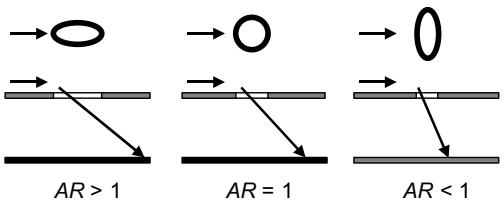

Fig. 6. Effects of aspect ratio on the touchdown locations of elliptic jets at the target plane.

direction, i.e., AR = 2, are shown in Fig. 5. Basically, the patterns of the spot distribution for the two aspect ratios are quite similar. However, the heat transfer performance of the impinging jet of AR = 0.5 is better than that of the jet of the aspect ratio AR = 2.

4.3. Effects of jet aspect ratio with flow exit at two ends (ExF-2)

To examine the effects of jet geometry on the heat transfer characteristics, Figs. 7 and 8 present the detailed Nusselt number distributions for elliptic jet arrays with ExF-2 condition and different aspect-ratios of the jet holes. The local Nusselt number distributions generated by jet arrays with AR $\leqslant 1$ are shown in Fig. 7 and the results with AR $\geqslant 1$ in Fig. 8. It is clearly observed that the shapes of the heat transfer spots of jet arrays in Fig. 7 are roughly resemble in general appearance, especially those with AR $\leqslant 1$ and 0.5. Overall inspection on Figs. 7 and 8 discloses that the best heat transfer performance is found for AR = 0.5 among five aspect ratios of elliptic jets under $Re = 3000$. In fact, it is found in the Table 1 that for $Re = 3000$ and 4500, the elliptic jets with

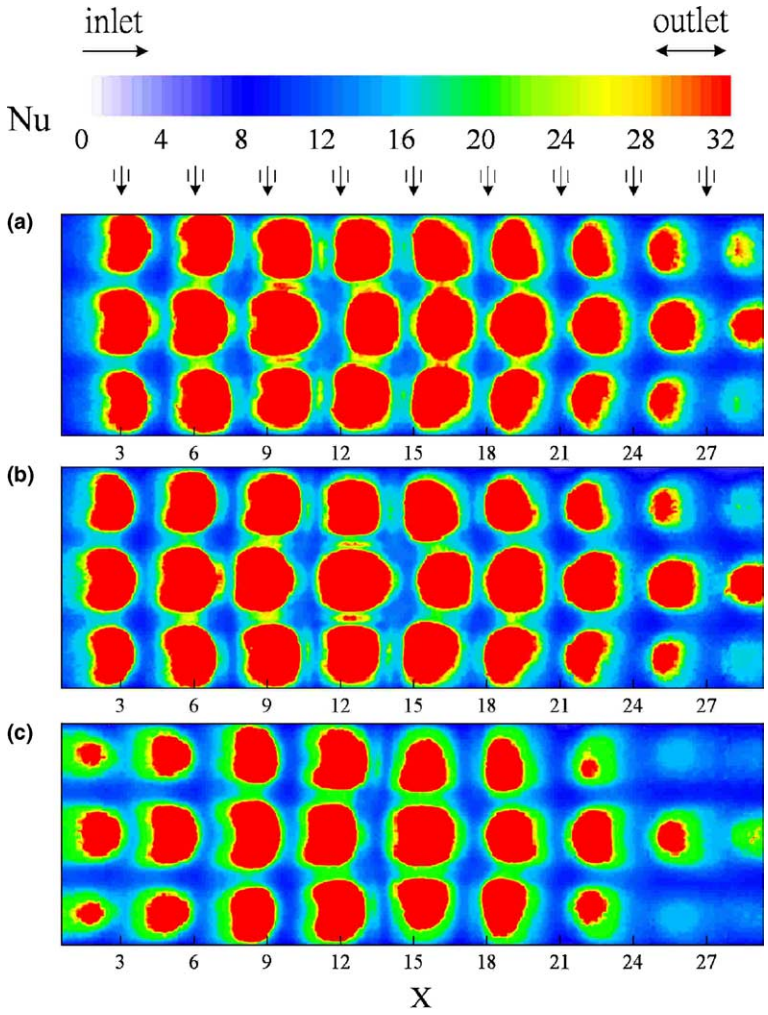

Fig. 7. Effects of aspect ratio AR on local Nusselt number distributions at $Re = 3000$, flow orientation 2 and $Z = 3$ with (a) AR = 1, (b) AR = 0.5, (c) AR = 0.25.

AR = 0.5 present a best heat transfer performance, while at low Reynolds number, $Re = 1500$, the mean heat transfer rate with AR = 2 and 1 becomes better than that with AR = 0.5. In Fig. 9, the present measurements of mean Nusselt number are compared with the previous data [10,11]. The present data provide information in a relatively lower Re range. It demonstrates that the heat transfer rates with one-way exit are obviously lower than those with two-way exit condition. Measured data from different sources show similar trend and the deviations seem limited in a reasonable range.

The shift of the touchdown location is also affected by the aspect ratio. In the case of AR > 1, the shift of the high-Nu spots can stem from two mechanisms. Since the major axis parallel to main stream in the pressure chamber (upper compartment in the test model), the jet issuing from the holes with an axial or X-component of inertial or momentum, it is the very inertial effect shift the impingement locations towards right. And this effect is less pronounced in the right region due to the presence of the right-end vertical plate in the pressure chamber, which renders the jets there issuing more downward and less X-component of momentum. On the other hand, the crossflow effects in the impingement chamber tend to sweep the jets towards the exits. For AR < 1, as explained with Fig. 6, the inertial effect is small and the crossflow effect dominates the shift of the jet impingement locations. While in the cases of AR > 1, the axial momentum is the more influential factor and the remarkable rightward shift of the high-Nu spot can be observed in the left part of the target plate. In the right part, the axial momentum effect is suppressed by the vertical end plate of the pressure channel. In this situation, therefore, the shift of the impingement location is also governed by the crossflow effect.

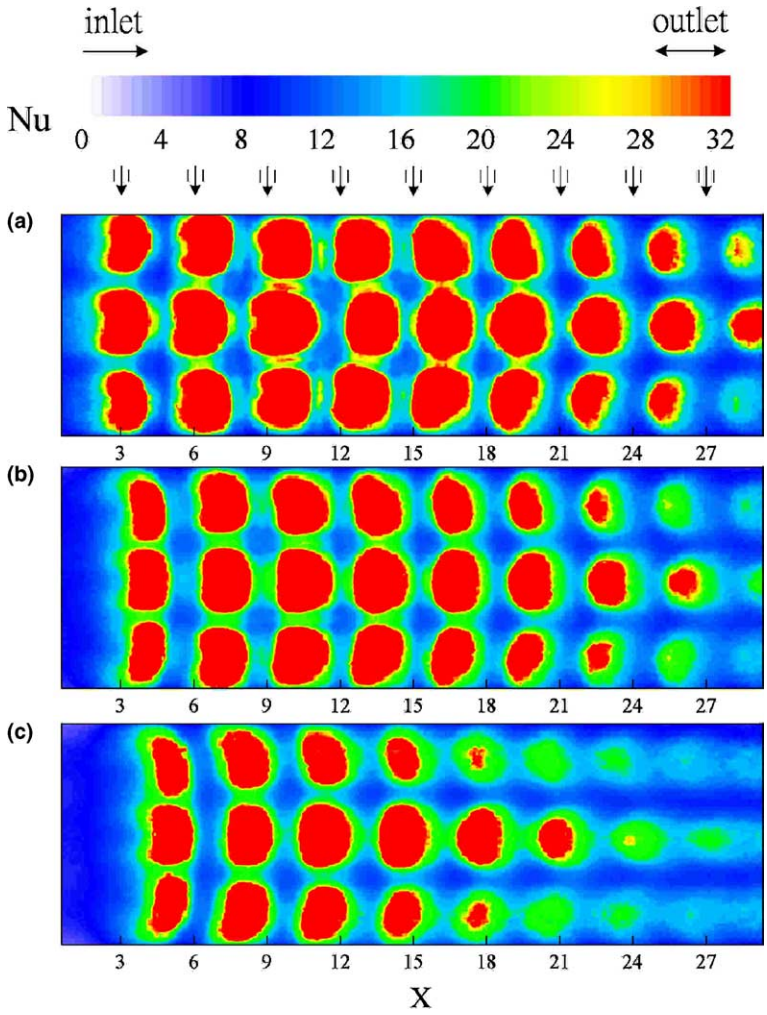

Fig. 8. Effects of aspect ratio AR on local Nusselt number distributions at $Re = 3000$, flow orientation 2 and $Z = 3$ with (a) AR = 1, (b) AR = 2, (c) AR = 4.

Table 1
Effects of aspect ratio AR and Reynolds number *Re* on the mean Nusselt number

Reynolds number	Aspect ratio		
	Mean Nusselt number, Nu_m		
	AR = 2	AR = 1	AR = 0.5
$Re = 4500$	35.021	43.955	44.669
$Re = 3000$	31.447	35.735	37.880
$Re = 1500$	16.617	16.152	14.723

4.4. Evolution of flow structure and axis-switchover in crossflow

Another striking feature is the shape of the high-*Nu* spots over the heat transfer surface or target plate. After the elliptic jet ejected from the jet hole and before it impinging on the target plate, it evolves to become likely circular, see the high-*Nu* spots in the middle region. However, approaching to the two exit ends, the increasingly strong crossflow tends to make the jet cross-section like a kidney shape of two-side swept towards downstream. In the left region, this phenomenon is more noticeable than that in the right part of the channel due to inherent asymmetry of flow condition in the upper compartment (pressure chamber).

For elliptic jet of AR > 1 with its major axis parallel to the channel axis, the high-*Nu* spots still develop their shapes with the long-side of the kidney-shape perpendicular to the major axis of the elliptic jet ports, especially in the leftmost region of the target plate. This consequence is related to the so-called axis-switchover

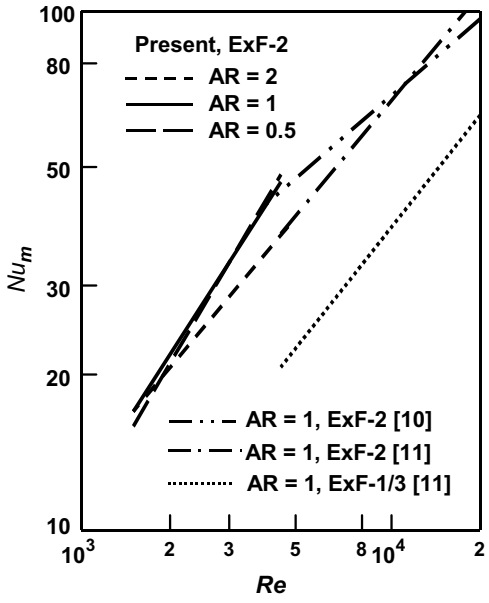

Fig. 9. Mean Nusselt numbers for impinging jet at various Reynolds numbers and exit flow conditions.

phenomenon mentioned in previous studies, e.g., [20], in which single free jets with axi-symmetric configuration were dealt with. However, the present elliptic jet array impingement with the presence of the crossflow is more complicated. Fig. 10 shows schematically the deformation of the cross-sectional shape of the elliptic jet of AR > 1 in the presence of two different crossflow conditions, counter-flow and co-flow. The elliptic jets issue from the jet holes at an inclined angle depending on the axial momentum and hole geometry. Then the jets evolve with inherent instability to perform axis-switchover. During the evolution, the influence of the crossflow tend to re-shape the elliptic cross-section to one with a concave side facing downstream. The resultant jet configuration of kidney-like shape is a consequence of the coupling effects of the jet hole geometry, jet momentum, axis-switchover and crossflow. It is important to note that the jets of AR < 1 still remain their long-side coincide with the hole major-axis. It means that the axis-switchover does not occur in this flow configuration with crossflow effects.

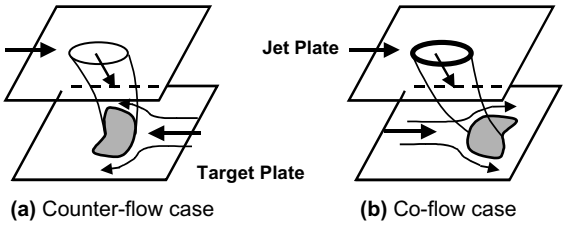

Fig. 10. Axis-switching of elliptic jets of AR > 1 in crossflow. (a) Counter-flow case; and (b) co-flow case.

5. Conclusions

In this work, local heat transfer characteristics on a target plate impinged by elliptic jet arrays have been analyzed based on the measurements by using a transient thermochromic liquid crystal technique. The present study focuses on the effects of the aspect ratio of elliptic jet arrays and exit flow orientation. The following points are the major findings in the parameter ranges considered in the present work.

1. The local Nusselt number distributions are significantly influenced by the crossflow. The best heat transfer performance can be obtained at the two-way exit condition of the spent flow diverted to the both ends of the impingement channel for the short traveling length and the lower deterioration stemmed from the crossflow effect.
2. For the elliptic jets of AR > 1, the shift of the jet touchdown locations in upstream portion of the impingement channel is dominated by the inertia of the jets, while that in the downstream the crossflow effect play dominant role. In the cases of AR < 1, the crossflow effect is the most influential factor to the shift of the impingement location.
3. Among the five aspect ratios considered, the mean heat transfer rates with the elliptic jets of AR = 0.5 are the best at $Re = 3000$ and 4500, While in the low-Re case. $Re = 1500$, the jet arrays with AR = 2 and 1 perform better than that with AR = 0.5.
4. The shape of high-Nu spots reflects the jet flow structure near the target plate. With crossflow effect, it is found that the cross-sections of the elliptic jets generally have a kidney-like shape but the shape is relatively fuller in the case with $AR \leqslant 1$. The resultant kidney-shape is a consequence of the coupling effects of hole geometry, jet momentum, axis-switchover and crossflow. For elliptic jet arrays with AR > 1, the axis-switchover occurs, while, in the presence of crossflow, this structure change cannot occur in the cases with $AR \leqslant 1$.
5. The flow and heat transfer mechanisms involved in the present elliptic jet array impingement is highly complicated. More profound investigations on the evolution of elliptic jet structure in the presence of a crossflow as well as the heat transfer enhancement with jet-crossflow–vortex interaction are most worthwhile.

Acknowledgment

The financial support of this study by the National Science Council of Taiwan, the R.O.C., through the grant number NSC 89-2212-E211-016, is gratefully acknowledged.

References

[1] K. Jambunathan, E. Lai, M.A. Moss, B. Button, A review of heat transfer data for single circular jet impingement, Int. J. Heat Fluid Flow 13 (1992) 106–115.
[2] R. Viskanta, Heat transfer to impinging isothermal gas and flame jets, Exp. Therm. Fluid Sci. 6 (1993) 111–134.
[3] L.W. Florschuetz, C.P. Truman, D.E. Metzger, Streamwise flow and heat transfer distribution for jet impingement with crossflow, ASME J. Heat Transfer 103 (1981) 337–342.
[4] L.W. Florschuetz, D.E. Metzger, C.C. Su, Y. Isoda, H.H. Tseng, Heat transfer characteristics for jet array impingement with initial crossflow, ASME J. Heat Transfer 106 (1984) 34–41.
[5] A.M. Huber, R. Viskanta, Effects of jet–jet spacing on convective heat transfer to confined, impinging arrays of axisymmetric air jets, Int. J. Heat Mass Transfer 37 (1994) 2859–2869.
[6] A.M. Huber, R. Viskanta, Comparison of convective heat transfer to perimeter and center jet in a confined, impinging array of axisymmetric air jets, Int. J. Heat Mass Transfer 37 (1994) 3025–3030.
[7] V.J.H. Lienhard, Liquid jet impingement, in: C.L. Tien (Ed.), Annual Review of Heat Transfer, vol. 6, Begell House, New York, 1995, pp. 199–270.
[8] C.H. Oh, V.J.H. Lienhard, H.F. Younis, R.S. Dahbura, D. Michels, Liquid jet-array cooling modules for high heat fluxed, AICHE J. 44 (1998) 769–779.
[9] K. Garrett, B.W. Webb, The effect of drainage configuration on heat transfer under an impinging liquid jet array, ASME J. Heat Transfer 121 (1999) 803–810.
[10] V. Treuren, K.W. Wang, Z. Ireland, T.V. Jones, Detailed measurements of local heat transfer coefficient and adiabatic wall temperature beneath an array of impingement jets, ASME J. Turbomachinery 116 (1994) 369–374.
[11] Y. Huang, S.V. Ekkad, J.C. Han, Detailed heat transfer distributions under an array of orthogonal impinging jets, AIAA J. Thermophys. Heat Transfer 12 (1998) 73–79.
[12] S.V. Ekkad, Y. Huang, J.C. Han, Impingement heat transfer on a target plate with film cooling holes, AIAA J. Thermophys. Heat Transfer 13c (1999) 522–528.
[13] G.S. Azad, Y. Huang, J.C. Han, Impingement heat transfer on dimpled surface using a transient liquid crystal technique, AIAA J. Thermophys. Heat Transfer 14 (2000) 186–193.
[14] C. Carcasci, An experimental investigation on air impinging jets using visualization methods, Int. J. Therm. Sci. 38 (1999) 808–818.
[15] W.M. Yan, H.C. Liu, C.Y. Soong, W.J. Yang, Experimental study of impingement heat transfer of incline and staggered jet arrays by using transient liquid crystal technique, J. Flow Visualization and Image Processing 10 (2003) 119–141.
[16] C.M. Ho, E. Gutmark, Vortex induction and mass entrainment in a small-aspect-ration elliptic jet, J. Fluid Mech. 179 (1987) 383–405.
[17] F. Hussain, H.S. Husain, Elliptic jets. Part 1. Characteristics of unexcited and excited jets, J. Fluid Mech. 208 (1989) 257–320.
[18] H.S. Husain, F. Hussain, Elliptic jets. Part 2. Dynamics of coherent structure paring, J. Fluid Mech. 233 (1991) 439.
[19] H.S. Husain, F. Hussain, Elliptic jets. Part 3. Dynamics of preferred mode coherent structure, J. Fluid Mech. 248 (1993) 315.
[20] S.J. Lee, J. Lee, D. Lee, Local heat transfer measurement from an elliptic jet impinging on a flat plate using liquid crystal, Int. J. Heat Mass Transfer 37 (1994) 967–976.
[21] J. Lee, S.J. Lee, The effect of nozzle aspect ratio on stagnation region heat transfer characteristics of elliptic impinging jet, Int. J. Heat Mass Transfer 43 (2000) 555–575.
[22] W.M. Yan, R.C. Hsieh, C.Y. Soong, Experimental study of surface-mounted obstacle effects on heat transfer enhancement by using transient liquid crystal thermography, ASME J. Heat Transfer 124 (2002) 762–769.